Decoupling Control of Bearingless Synchronous Reluctance Motor Based on SVM Inversely Optimized by ACO

Xiaoyan Diao, Huangqiu Zhu

School of Electrical and Information Engineering, Jiangsu University, Zhenjiang 212013, China

(dxy@ujs.edu.cn; zhuhuangqiu@ujs.edu.cn)

Abstract

Based on the SVM inversely optimized by ant colony optimization (ACO), this paper proposes a decoupling control approach for the bearingless synchronous reluctance motor (BSRM), a multivariable, nonlinear and strong-coupled system. Specifically, the inverse model approximated by SVM based on the ACO was cascaded with the original system to obtain three composite pseudo-linear subsystems, and the closed-loop controllers were designed for these pseudo-linear subsystems. The simulation results proved the effectiveness of the decoupling control strategy, and evidenced the dynamic performance and robustness of the control system.

Key words

Bearingless synchronous reluctance motor, Support vector machine, Ant colony optimization algorithm, Decoupling control.

1. Introduction

Over the years, increasing attention has been paid to bearingless motors with built-in magnetic bearings, particularly the bearingless synchronous reluctance motor (BSRM). Featuring simple structure, low cost, stable temperature, fast speed and high precision [1-3], the BSRM enjoys tremendous application potential in special fields like aerospace, life science, new energy and fine chemical industry [4]. As a typical multivariable nonlinear system, the BSRM exhibits strong coupling among the electromagnetic torque and the radial suspension forces in x- and y-directions, making it necessary to develop a dynamic decoupling control strategy.

Recent years has witnessed the birth of some decoupling methods for the BSRM. The first decoupling strategy was proposed in [5-6] based on a series feed-forward compensator. However,

the control effect is poor, as the compensator parameters are easily swayed by the magnetic saturation. Inspired by this strategy, presented an improved mathematical model that reduces the magnetic saturation and the coupling among the electromagnetic torque and two radial forces through approximation, online table look-up and real-time parameters detection [7]. Despite the fulfillment of the static decoupling, the model fails to achieve the dynamic decoupling control. Other decoupling approaches include the inverse system method and the neural network method. Nevertheless, the former works only if the mathematical model of the system and the corresponding inverse model are given [8], and the latter is weak on generalization owing to inherent defects of low learning speed, convergence to local minimum, and over-fitting [9].

A possible way to tackle the above problems lies in the support vector machine (SVM). As a powerful machine learning technique based on the statistical learning theory, the SVM can resolve such problems as small sample size, over-fitting, high dimensionality, poor generalization and convergence to local minimum, following the principle of structural risk minimization [10]. The learning results and generalization ability of the SVM directly hinge on the accuracy of the parameters. Hence, the SVM was inversely optimized by the ant colony optimization (ACO) algorithm, a heuristic optimization method that obtains the optimal solutions based on the paths of artificial ants. On this basis, the author proposed a dynamic decoupling control method for the BSRM. The proposed method identifies the inverse system of the original nonlinear system by the SVM, and cascades the inverse model with the original system to form a decoupled pseudo-linear system. In light of the single-input single-output system theory, it is possible to design the closed-loop controller of the decoupled pseudo-linear system.

2. Operation Principle and Mathematical Model of the BSRM

2.1 Operation Principle of the BSRM

Figure 1 illustrates the generation of radial suspension forces in the BSRM under no-load condition. The BSRM combines torque windings and suspension force windings in one stator.

As shown in Figure 1, when the current passes 4-pole torque windings N_a and 2-pole suspension force windings N_x and N_y, the 4-pole torque windings N_a generate flux linkage ψ_a and the 2-pole suspension force windings N_x and N_y respectively generate flux linkage ψ_x and ψ_y. When currents are applied on the suspension force windings, the flux density will increase in area 2 but decrease in area 4. The unbalanced magnetic fields will result in the radial force F_x in the positive x-direction, and similarly the radial force F_y in the positive y-direction. Thus, the magnitude and direction of the radial suspension forces can be controlled by adjusting the currents in the two sets of windings, laying the basis for achieving stable suspension of the rotor.
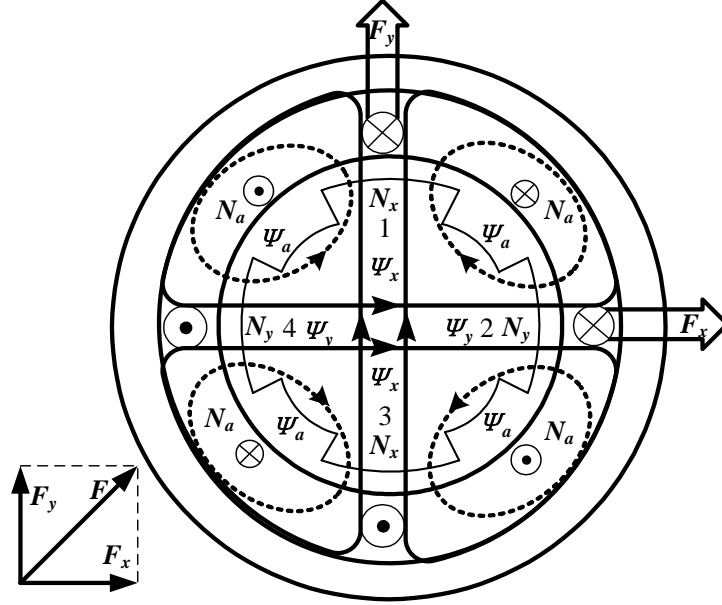
Fig.1. Generation of Radial Forces in the BSRM

2.2 Description of the Mathematical Model

Whereas the BSRM has a salient-pole rotor, only the effective part of the salient regions is considered in the calculation of the radial suspension forces. The pole arc is assumed as 30°, the pole pair number of torque windings P_M as 2, and the pole pair number of suspension force windings P_B as 1. The magnetic saturation is neglected. The mathematical models of torque subsystem and radial force subsystem can be deduced by the Maxwell stress tensor method [11].

The radial suspension forces on the rotor can be derived as

$$
\begin{bmatrix} F_x \\ F_y \end{bmatrix} = \begin{bmatrix} K_{m1}i_d & K_{m2}i_q \\ K_{m2}i_q & -K_{m1}i_d \end{bmatrix} \begin{bmatrix} i_x \\ i_y \end{bmatrix}
$$
$$
= \begin{bmatrix} K_{m1}i_d & K_{m2}i_q \\ K_{m2}i_q & -K_{m1}i_d \end{bmatrix} \begin{bmatrix} \cos 2\theta & -\sin 2\theta \\ \sin 2\theta & \cos 2\theta \end{bmatrix} \begin{bmatrix} i_{2\alpha} \\ i_{2\beta} \end{bmatrix} \tag{1}
$$

where $K_{m1} = \frac{\mu_0 lr N_2 N_4}{48\delta_0^2}(2\pi + 3\sqrt{3})$; $K_{m2} = \frac{\mu_0 lr N_2 N_4}{48\delta_0^2}(2\pi - 3\sqrt{3})$; i_d and i_q are respectively the equivalent two-phase currents of the torque windings along the two axes in d-q synchronous reference frame; i_x and i_y are respectively the equivalent two-phase currents of suspension force windings along the two axes in d-q synchronous reference frame; l is the stack length; μ_0 is the vacuum permeability; r is the rotor radius; N_2 and N_4 are respectively the number of per-phase effective turns in series of the torque windings and suspension force windings; θ is the mechanical rotor angle; $i_{2\alpha}$ and $i_{2\beta}$ are respectively the currents of suspension force windings along the two axes in the stationary coordinate system.

In addition, when the rotor deviates from the stator centre, the rotor will produce Maxwell stress which is directly proportional to the eccentric displacement:

$$\begin{bmatrix} F_{sx} \\ F_{sy} \end{bmatrix} = k \frac{\pi r l B^2}{\mu_0 \delta_0} \begin{bmatrix} x \\ y \end{bmatrix} = K_s \begin{bmatrix} x \\ y \end{bmatrix} \tag{2}$$

where k is the motor structure factor; B is the flux density amplitude in the airgap.

Assume that F_{zx} and F_{zy} are the interference forces on the rotor in x- and y-direction, respectively. Considering the two forces and gravity, the motion equations of the radial force subsystem are expressed as

$$\begin{cases} -F_x + F_{sx} + F_{dx} = m\ddot{x} \\ -F_y + F_{sy} + F_{dy} = m\ddot{y} \end{cases} \tag{3}$$

Then, the electromagnetic torque can be obtained by:

$$T_e = \frac{3}{2} P_M (L_d - L_q) i_d i_q \tag{4}$$

Hence, the motion equation of the torque subsystem is expressed as:

$$T_e - T_L = \frac{J}{P_M} \frac{d\omega}{dt} \tag{5}$$

where T_e is the electromagnetic torque; P_M is the pole pair number of the torque windings; L_d and L_q are respectively the inductances of the torque windings along the two axes in d-q synchronous reference frame; ω is the synchronous electrical angular speed; J is the moment of inertia; T_L is the load torque.

3. Decoupling Control Based on SVM Inversely Optimized by ACO

3.1 Reversibility Analysis for the Original System of the BSRM

Based on the above mathematical model, it is known that the BSRM is a multi-input- multi-output (MIMO) nonlinear system. The system state is defined as:

$$\mathbf{X} = \begin{bmatrix} x_1 & x_2 & x_3 & x_4 & x_5 \end{bmatrix}^T = \begin{bmatrix} x & y & \dot{x} & \dot{y} & \omega \end{bmatrix}^T \tag{6}$$

First, the input state is defined as:

$$\mathbf{U} = \begin{bmatrix} u_1 & u_2 & u_3 \end{bmatrix}^{\mathrm{T}} = \begin{bmatrix} i_q & i_x & i_y \end{bmatrix}^{\mathrm{T}} \tag{7}$$

Then, the output state is given as:

$$\mathbf{Y} = \begin{bmatrix} y_1 & y_2 & y_3 \end{bmatrix}^{\mathrm{T}} = \begin{bmatrix} x & y & \omega \end{bmatrix}^{\mathrm{T}} \tag{8}$$

According to the mathematical model, the state equation of the BSRM can be derived as:

$$\dot{\mathbf{X}} = f(\mathbf{X}, \mathbf{U}) = \begin{cases} \dot{x}_1 = x_3 \\ \dot{x}_2 = x_4 \\ \dot{x}_3 = \dfrac{1}{m}(-K_{m1}i_d u_2 - K_{m2}u_1 u_3 + k_s x_1 + F_{zx}) \\ \dot{x}_4 = \dfrac{1}{m}(-K_{m2}u_1 u_2 + K_{m1}i_d u_3 + k_s x_2 + F_{zy}) \\ \dot{x}_5 = \dfrac{3P_{\mathrm{M}}^2}{2J}(L_d - L_q)i_d u_1 - \dfrac{P_{\mathrm{M}}}{J}T_L \end{cases} \tag{9}$$

Based on the interactor algorithm, the reversibility of the system is analysed by differentiating the output function y=h(x)=[x$_1$ x$_2$ x$_5$]$^{\mathrm{T}}$ until it explicitly includes the input state **U**. The Jacobian matrix can be calculated as:

$$\mathbf{A}(\mathbf{X}, \mathbf{U}) = \begin{bmatrix} -\dfrac{1}{m}K_{m2}u_3 & -\dfrac{1}{m}K_{m1}i_d & -\dfrac{1}{m}K_{m2}u_1 \\ -\dfrac{1}{m}K_{m2}u_2 & -\dfrac{1}{m}K_{m2}u_1 & \dfrac{1}{m}K_{m1}i_d \\ \dfrac{3P_{\mathrm{M}}^2}{2J}(L_d - L_q)i_d & 0 & 0 \end{bmatrix} \tag{10}$$

The determinant of the Jacobian matrix **A** is:

$$\det\mathbf{A} = -\frac{3P_{\mathrm{M}}^2 i_d}{2m^2 J}(L_d - L_q)(K_{m1}^2 i_d^{\,2} + K_{m2}^2 u_1^2) \tag{11}$$

It is obvious that det **A**≠ 0, indicating that the matrix **A** is non-singular. The relative degrees of the system are α=(α$_1$,α$_2$,α$_3$)=(2,2,1), where α$_1$+α$_2$+α$_3$=5=n (the dimension of the system). Thus, the system is reversible.

3.2 SVM Training and ACO-based Optimization

Following the statistic learning theory and the principle of structural risk minimization, the

SVM can overcome the problems like small sample size and convergence to local minima. The basic idea of the SVM is to map the training data to a high-dimensional feature space. To make the undivided linear sample space linearly separable, the constructive nonlinear kernel mapping is employed to map the original data space to a high-dimensional feature space.

The output of the SVM is obtained as

$$f(\boldsymbol{x}) = \sum_{i=1}^{k} (\alpha_i^* - \alpha_i) \boldsymbol{K}(\boldsymbol{x}, x_i) + b \qquad (12)$$

where $K(x, x_i)$ is the kernel function of the SVM; α_i^* and α_i are the Lagrange multipliers; b is threshold obtained by combining KKT conditions.

There are many different kernel functions, which form the various algorithms in the SVM. In this research, the Gaussian function below is taken as the kernel function.

$$\boldsymbol{K}(\boldsymbol{x}, x_i) = \exp(-\|\boldsymbol{x} - x_i\|^2 / 2\sigma^2) \qquad (13)$$

The SVM-based identification of the inverse model of the original system is detailed in [12]. In spite of the perfect theoretical basis, the SVM still faces some problems in practice, such as the determination of parameters like the penalty factor C and the parameter of kernel function σ, two key determinants of the classification accuracy. Thus, the ACO was introduced to optimize these parameters.

The ACO offers an effective tool to solve multi-objective optimization problems [13]. The novel heuristic optimization method is known for intelligent search, global optimization and strong robustness [14]. In this paper, the optimal solutions of C and σ are obtained in continuous space domain. The SVM parameters are optimized in the following steps:

(1) Initialize the parameters C and σ, denote the number of ants as m, and set the maximum iteration and initial value ranges of the parameters.

(2) Mesh the parameter optimization region into grids, so that the ants are able to move in each grid point and leave behind pheromones.

(3) Train the SVM, compute the objective function, and update the amount of pheromone.

(4) Figure out the state transition probability of the ants, transfer the ants to grid points with the maximum probability, and record the amount of pheromone at these points.

(5) Repeat Step (4) until reaching the maximum iteration.

(6) Narrow down the range of variables as far as the high pheromone points are concerned, and perform ant colony migration within the scope of small grids.

(7) Repeat Steps (2) ~ (6) until the difference of objective functions satisfies the relevant requirements and a global optimal path can be obtained.

(8) Calculate the corresponding optimal parameters (C & σ) and use the optimized parameters to train SVM.

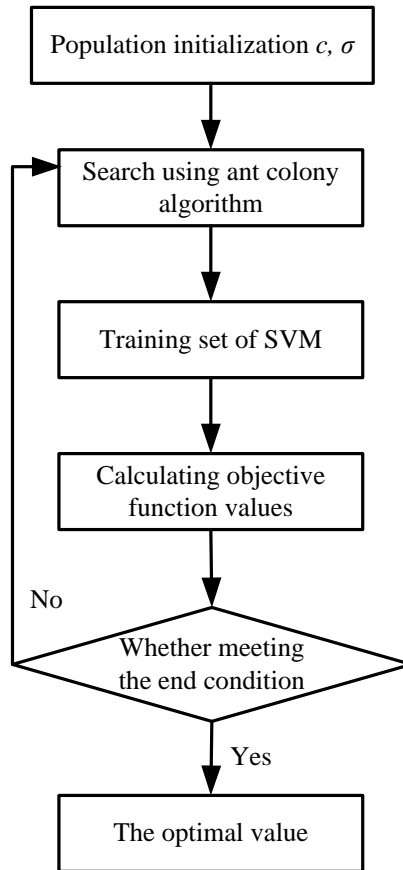Figure 2 details the steps of the ACO-based SVM parameter optimization.

Fig.2. ACO-based SVM Parameter Optimization

3.3 Construction and Control of the Inverse System

100 groups of input and output data were obtained by adding uncorrelated white noise to the input ports. These data were taken as the training sample sets.

The fitting factors are assumed as below:

$$
\begin{cases}
X_1 = [\dot{\omega} \quad n] \\
X_2 = [\ddot{x} \quad \dot{x} \quad i_q \quad i_y \quad y] \\
X_3 = [\ddot{y} \quad \dot{y} \quad i_q \quad i_x \quad x]
\end{cases}
\tag{14}
$$

These data were trained by SVM method to obtain the corresponding factor a_i^j and threshold

b_j of the input vector u_j. Based on the current input, the inverse system of the BSRM can be expressed as:

$$u_j = \sum_{i=1}^{k} \left(a_i^{j^*} - a_i^{j} \right) K(x_i^j, x_j) + b_j \ (j = 1, 2, 3)$$

(15)

Then, the ACO was introduced to optimize the SVM parameters. The ACO parameters are set as follows: the number of ants $m=20$, the maximum cycle index $N_{max}=100$, the value range of C [0, 10,000], the value range of σ [0.1, 100], and the pheromone density $\rho=0.7$. With the k-fold cross validation error as the target value, three SVMs were trained with the ACO, and the optimal solution C and σ were obtained as: $C_1=2,300$, $\sigma_1=2.16$, $C_2=C_3=4,500$ and $\sigma_2=\sigma_3=6$.

The identified inverse system of the BSRM was then cascaded with the original system, forming a compound pseudo-linear system. Under the effect of multiple factors, the compound pseudo-linear system is not an ideal linear system in practice. With this consideration, an additional controller was designed to compose a feedback control system. In this research, the PID controller is adopted to design closed-loop linear controller (Figure 3).
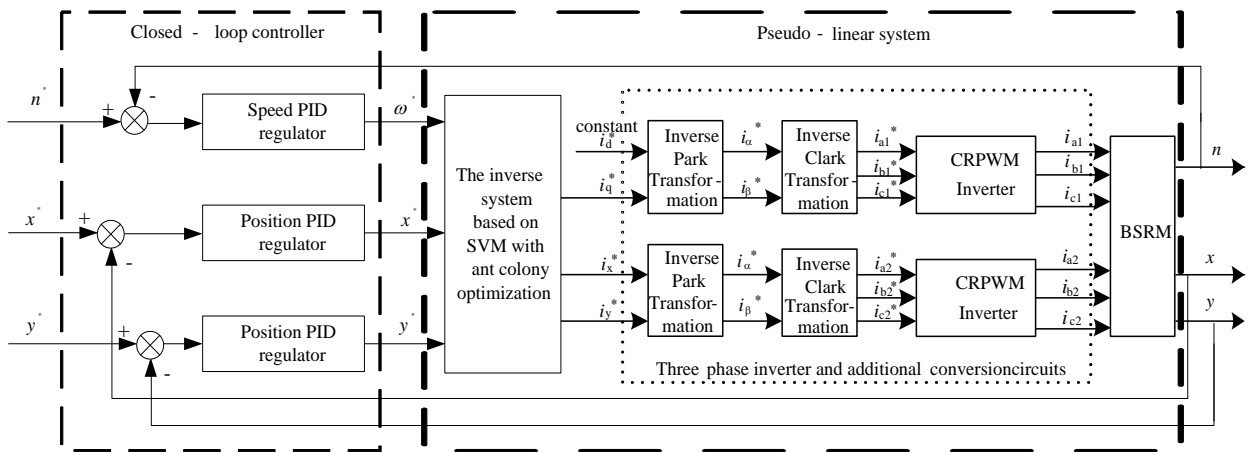

Fig.3. Structure of The Closed-Loop Linear Controller
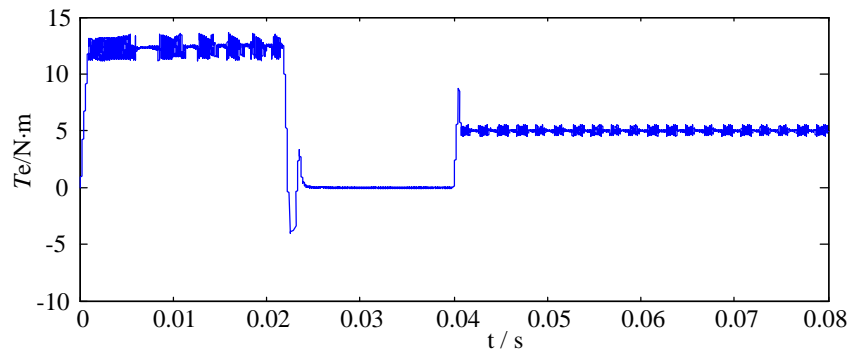
4. Simulation Research

In order to verify the effectiveness of the proposed decoupling control method, a simulation model was constructed based on MATLAB Simulink platform. The motor parameters are as follows: motor power 300W, rotor mass $m=1$kg, moment of inertia of motor $J = 0.002$kg·m^2, airgap length $\delta_0=0.25$mm, stator resistance $R_{s1}=0.25\Omega$, pole pair number of torque winding $P_M=2$, inductance of torque winding $L_d=0.035$H and $L_q=0.0042$H, pole pair number of suspension force winding $P_B=1$, inductance of suspension force winding $L_x=L_y=0.02$H, and stator resistance

R_{s2}=0.15Ω.
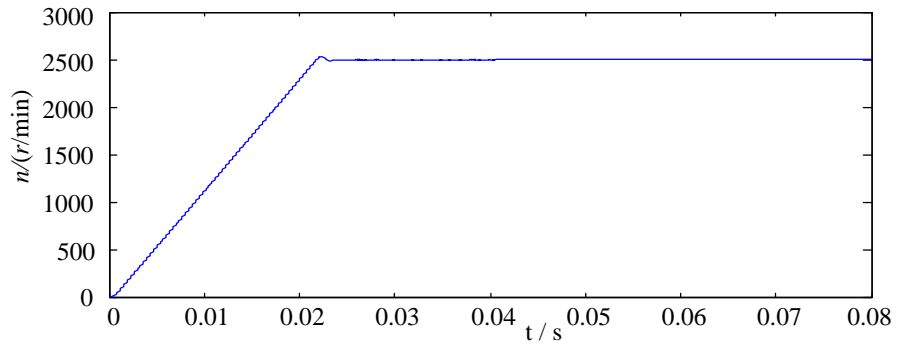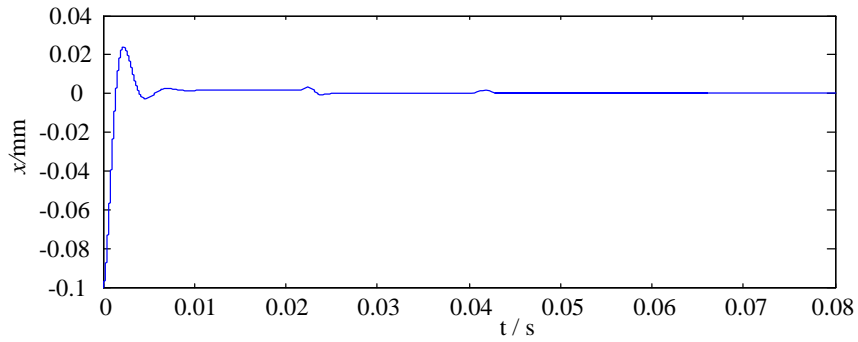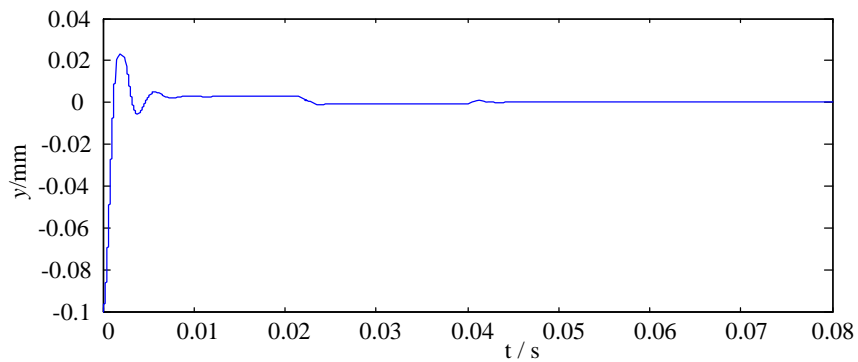

(a) Speed Curve

(b) Torque Curve

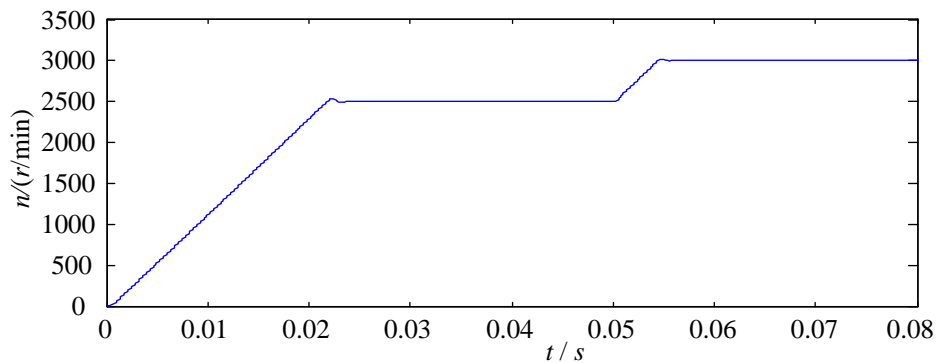(c) Displacement Curve in *x*-direction

(d) Displacement Curve in *y*-direction

Fig.4. Simulation Results of Decoupling Control on the BSRM

224

According to the step response curve of speed in Figure 4(a), the adjustment time of speed was about 0.023s, and the overshoot is about 1.5%. It indicates that the system has good speed performance.

The torque response curve is shown in Figure 4(b). When the motor started in the no-load condition, the torque jumped to 0 after the motor entered the smooth operation. The torque $T_L=5N·m$ was given at $t=0.04$s. In the event of transient small fluctuations, the pre-set torque was achieved very quickly. This means the torque subsystem has a good dynamic and static performance.

Figure 4(c) and 4(d) present the displacement curves in x- and y-directions, respectively. The initial values of the rotor position were set as $x_0=$ -0.1 mm and $y_0=$ -0.1 mm, and the reference rotor displacements were configured as $x^*=0$ mm and $y^*=0$ mm. As shown in the two figures, the rotor arrived at the reference positions from start-up, and achieved stable suspension in the central position. The torque change at t=0.04s had virtually no impact on the displacements in x- and y-directions. It is clear that the proposed decoupling method removes the coupling between the electromagnetic torque and radial suspension forces.

(a) Response Curve of Speed
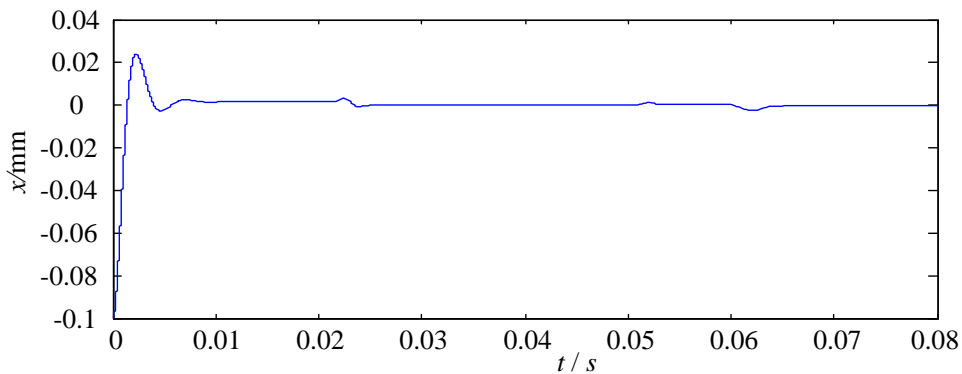
(b) Displacement Curve in x-direction
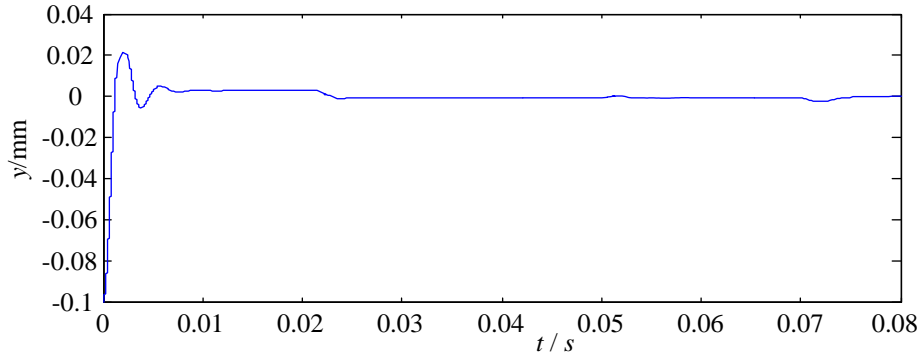
(c) Displacement Curve in y-direction

Fig.5. Simulation Results with External Disturbance

Figure shows the simulation results with external disturbance. The reference speed of rotor varies from 2,500r/min to 3,000r/min at t=0.05s. As shown in Figure 5(a), the speed reached the given reference of 3,000r/min in 4ms. According to Figure 5(b) and 5(c), the displacements fluctuated slightly at 0.05s in both x- and y-directions. When the motor rotated smoothly at the speed of 3,000r/min, the external disturbances in x- and y-directions F_{zx}'=20Nm, F_{zy}'=20Nm were added on the rotor at t=0.06s and t=0.07s, respectively. As shown in Figure 5, when the radial displacements in x- and y-directions were disturbed, respectively, the displacements quickly returned to the pre-set values, and seldom affected each other. The phenomenon reveals that the electromagnetic torque and the radial suspension forces are decoupled successfully, and that the proposed control method boasts good disturbance resistance.

Conclusion

Based on the SVM inversely optimized by ACO, this paper presents a decoupling control approach for the BSRM. The method manages to achieve the dynamic decoupling control among the electromagnetic torque and the radial suspension forces in x- and y-directions. The simulation results demonstrate that the proposed control strategy boasts quick response, good dynamic and static characteristics, and disturbance resistance despite external disturbance.

Acknowledgments

References

1. G.H.B. Foo, X. Zhang, Robust Direct Torque Control of Synchronous Reluctance Motor Drives in the Field-Weakening Region, 2016, IEEE Trans. On Power Electronics, vol. 32, no. 2, pp. 1289-1298.

2. N. Boubaya, B. Saad, M. Maazouz, Radial active magnetic bearing control using fuzzy logic, 2016, Modelling, Measurement and Control A, vol. 89, no. 1, pp. 92-100.

3. S.E. Saarakkala, M. Sokolov, M. Hinkkanen, J. Kataja, K. Tammi, State-Space Flux-Linkage Control of Bearingless Synchronous Reluctance Motors,2016, IEEE Energy Conversion Congress & Exposition (ECCE), Milwaukee, USA, no. 16671888.

4. V. Mukherjee, J. Pippuri, S.E. Saarakkala, Finite Element Analysis for Bearingless Operation of a Multi Flux Barrier Synchronous Reluctance Motor2015, International Conference on Electrical Machines and Systems, Pattaya, Thailand, pp. 688-691.

5. C. Michioka, T. Sakamoto, O. Ichikawa, A. Chiba, A decoupling control method of reluctance-type bearingless motors considering magnetic saturation, 1996, IEEE Trans. on Industry Applications., vol. 32, no. 5, pp. 1204-1210.

6. H. Zhang, H. Zhu, X. Diao, Feedback decoupling control of bearingless synchronous reluctance motor, 2007, Proc. of the 26th Chinese Control Conference, pp. 763-767.

7. L. Hertle, Hofmann W., Magnetic couplings in a bearingless reluctance machine, 2000, Proc. of the International Conference on Electrical Machines, vol. 16, no. 5, pp. 1776-1780.

8. T. Zhang, H. Zhu, Decoupling control based on inverse system for bearingless synchronous reluctance motor, 2011, Control Theory & Applications, vol. 28, no. 4, pp. 545-550.

9. X. Sun, L. Chen, Z. Yang, W. Zhang, High-Performance control for a bearingless permanent-magnet synchronous motor using neural network inverse scheme plus internal model controllers, 2016, IEEE Trans. on Industrial Electronics., vol. 63, no. 6, pp. 3479-3488.

10. X. Li, A. Zhang, X. Zhang, C. Li, L. Zhang, Rolling element bearing fault detection using support vector machine with improved ant colony optimization, 2013, Measurement, vol. 46, no. 8, pp. 2726-2734.

11. A. Chiba, T. Fukao, M. Rahman, An analysis of bearingless AC motors, 1994, IEEE Trans. On Energy Conversion, vol. 9, no. 1, pp. 61-68.

12. H. Zhu, Y. Li, L. Cao, Decoupling control of bearingless synchronous reluctance motor based on least squares support vector machines, 2012, Control and Decision, vol. 27, no. 11, pp. 1663-1668.

13. Q. Wu, L. Tang, H. Li, L. Ouyang, A co-evolutionary particle swarm optimization with dynamic topology for solving multi-objective optimization problems, 2016, Advances in Modelling and Analysis A, Vol. 53, No. 1, pp. 145-159.

14. X. Zhang, W. Chen, B. Wang, X. Chen, Intelligent fault diagnosis of rotating machinery using support vector machine with ant colony algorithm for synchronous feature selection and parameter optimization, 2015, Neurocomputing, vol. 167, pp. 260-279.